Article

Intrinsic Conductance of Ferroelectric Charged Domain Walls

Feng Yang

School of Materials Science and Engineering, University of Jinan, Jinan 250022, China; mse_yangf@ujn.edu.cn

Abstract: Ferroelectric charged domain walls offer a revolutionary path for next-generation ferroelectric devices due to their exceptional conductivity within an otherwise insulating matrix. However, quantitative understanding of this "giant conductivity" has remained elusive due to the lack of robust models describing carrier behavior within CDWs. The current paper bridges this critical knowledge gap by employing a first-principles approach that incorporates Boltzmann transport theory and the relaxation time approximation. This strategy enables the calculation of carrier concentration, mobility, and conductivity for both head-to-head and tail-to-tail domain wall configurations within a stabilized periodic structure. The comprehensive transport analysis given here reveals that the accumulation of charge carriers, particularly their concentration, is the dominant factor governing domain wall conductance. Interestingly, observed conductance differences between head-to-head and tail-to-tail walls primarily arise from variations in carrier mobility. Additionally, this study demonstrates a significantly reduced domain wall width compared to previous reports. This miniaturization is attributed to the presence of compressive strain, which lowers the energy barrier for electron–hole pair generation. Furthermore, the findings here suggest that reducing the band gap presents a viable strategy for stabilizing charged domain walls. These results pave the way for the optimization and development of domain wall devices across a spectrum of ferroelectric materials.

Keywords: charged domain wall; conductance; ferroelectrics; thin films; first principles

Citation: Yang, F. Intrinsic Conductance of Ferroelectric Charged Domain Walls. *Physics* **2024**, *6*, 1083–1097. https://doi.org/10.3390/physics6030067

Received: 11 April 2024
Revised: 11 July 2024
Accepted: 13 August 2024
Published: 29 August 2024

Copyright: © 2024 by the author. Licensee MDPI, Basel, Switzerland. This article is an open access article distributed under the terms and conditions of the Creative Commons Attribution (CC BY) license (https://creativecommons.org/licenses/by/4.0/).

1. Introduction

Ferroelectric materials stand out for their ability to retain an electric polarization even without an external electric field. These materials can exist in two stable polarization states, which are switchable using electric fields [1]. Within a ferroelectric sample, regions with different polarization orientations, called domains, coexist and are separated by domain walls (DWs)—boundaries between regions with different polarization orientations (Figure 1). These DWs are essentially ultra-thin interfaces, just a few nanometers thick [2,3]. Interestingly, a domain wall can accumulate a net polarization charge, transforming it into a charged domain wall (CDW). This transformation unlocks a fascinating property: significantly enhanced conductivity. This phenomenon, akin to a localized metal–insulator transition [4,5], has been observed in various ferroelectric semiconductors like $BiFeO_3$, $BaTiO_3$, $LiNbO_3$, and $PbZr_xTi_{1-x}O_3$, in both thin films and crystals [6–10]. The enhanced conductivity of CDWs is attributed to the uncompensated polarization charges (positive or negative) residing within them. These polarization charges generate a local electric field that attracts free carriers, boosting the overall conductivity of DWs [11]. Notably, head-to-head (HH) CDWs exhibit a remarkable ability to amass a large number of carriers, leading to a dramatic increase in conductivity—sometimes by several orders of magnitude. For instance, $BaTiO_3$ DWs show a staggering 10^9-fold enhancement [7,12]. In $LiNbO_3$, this translates to a conductance 10 orders of magnitude higher than the bulk material, with charge carriers confined to nanoscale sheets [13]. Another intriguing aspect of DWs is their controllability. By applying an electric field, one can create, erase, or manipulate the position of CDWs within the material [14,15]. This precise control, coupled with the dramatic conductivity enhancement at these nanoscale regions, makes charged domain

walls highly attractive for developing future electronic devices [16]. These devices could include junctions, memory elements, diodes, logic gates, and memristors [17–20].

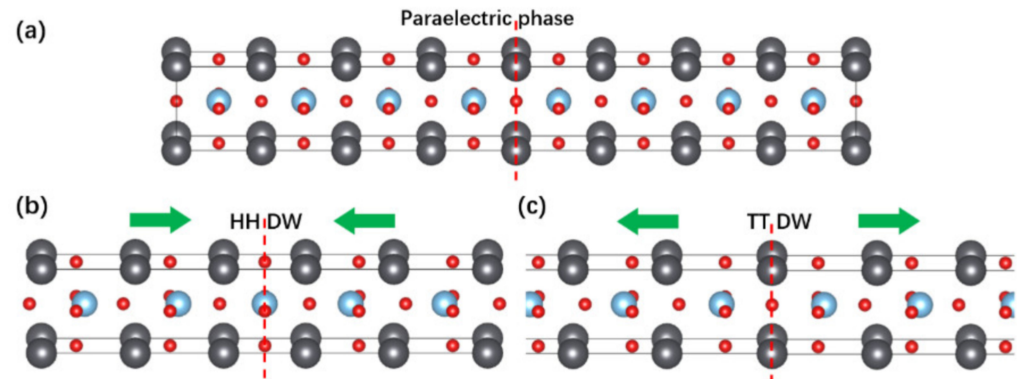

Figure 1. Schematic representation of (**a**) paraelectric phase, (**b**) head-to-head (HH) domain wall (DW), and (**c**) tail-to-tail (TT) domain wall. Atoms are represented by spheres: O (red), Pb (grey), and Ti (light blue). The green arrows indicate the direction of polarization.

The precise mechanisms governing DW conduction remain a topic of active research, with material-specific variations influencing the dominant factors [21]. Researchers have broadly categorized these mechanisms into intrinsic and extrinsic effects. Intrinsic mechanisms propose that structural changes within the DW create a polarization discontinuity. This discontinuity leads to disruptions in the electrostatic potential, manifesting as band bending or band gap reduction within the DW region [2,22,23]. The type of polarization discontinuity (HH or tail-to-tail (TT)) determines whether electron or hole conduction is favored through band modulation [24–26]. The intrinsic mechanism, relying solely on band modulation within the DW, offers potential advantages such as ultrafast response times and inherent resistance to degradation from defects, compared to the extrinsic mechanism. In contrast, extrinsic DW conduction relies on point defects. These charged defects can segregate towards or away from DWs, attracting or repelling charge-compensating carriers (electrons or holes) to maintain electrical neutrality [9,27–29]. However, real materials often exhibit a complex interplay between both intrinsic and extrinsic mechanisms, making it challenging to isolate their respective contributions. Furthermore, the evaluation of DW-specific responses is hindered by the lack of comprehensive data on fundamental electronic properties like carrier concentrations (electron n and hole p) and mobilities (μ) [30].

Understanding the transport properties of ferroelectric DWs is critical for their application in next-generation devices. These properties, particularly the concentration and mobility of majority charge carriers, remain elusive due to limitations in current experimental techniques [13,30]. Quantifying carrier concentration and mobility within DWs remains a significant challenge [13,18,31–34]. Accurately measuring even the most common parameter, intrinsic DW conductivity, is also hindered by several factors [35]. In ferroelectric thin film devices, the interface between the film and the electrode forms a Schottky barrier. This barrier complicates the separation of true DW conduction from the contribution of the interface to the overall measured current. This effect becomes more pronounced in thicker films. The current flowing through DWs can vary significantly between devices fabricated with the same ferroelectric material. This inconsistency is attributed to the influence of randomly distributed defects within the film. These defects lead to poor reproducibility and an unreliable ON/OFF current ratio. The defect concentration on the thin film surface not only alters the state of the interfacial barrier but also significantly affects how defects inject and trap charge under an applied electric field. This, in turn, strongly influences the measured DW current. Therefore, theoretical research that sheds light on the concentration and mobility of the carriers within DWs is highly desirable. Such research can complement experimental efforts and pave the way for the development of next-generation ferroelectric devices.

This study presents a groundbreaking approach that leverages first-principles calculations in conjunction with Boltzmann transport theory. This combined method allows us to predict the mobility and concentration of charge carriers within both HH and TT CDWs. Importantly, the simulations applied here capture the intrinsic properties of the materials, eliminating the influence of confounding factors like defects or dopants. By calculating both carrier concentration and mobility, one can comprehensively determine the conductivity of the CDWs. This study represents the first systematic first-principles investigation of conductance in ferroelectric CDWs, offering valuable insights into the fundamental behavior of charge carriers within these materials.

2. Definitions and Methods

First-principles calculation was performed within the framework of density functional theory (DFT) [36,37] based on the Vienna ab initio simulation package [38–40]. Exchange and correlation effects were treated with the local density approximation (LDA) [41] to simulate the eight-unit periodic structure containing both HH and TT 180° CDWs in $PbTiO_3$. Furthermore, the generalized gradient approximations (GGA) [42] with Perdew–Burke–Ernzerhof (PBE) parameterization was employed as the exchange-correlation potential to calculate the polarization in the ferroelectric domain. Specifically, the valence electron configurations of O ($2s^2$ $2p^4$), Ti ($3s^2$ $3p^6$ $3d^2$ $4s^2$), and Pb ($5s^2$ $5p^6$ $5d^{10}$ $6s^2$ $6p^2$) were considered. A plane-wave cutoff energy of 630 eV was used. As shown in Figure 1a, a periodically repeated tetragonal ($1 \times 1 \times l$) supercell with the composition $(PbO\text{-}TiO_2)_l$ (l = 8) was employed to model both DW structures. Initially, an ideal structure was constructed by stacking m unit cells of $PbTiO_3$ along the [001] direction in a tetragonal ferroelectric configuration. Both sides possessed polarization vectors converging towards the center. Subsequently, a stable structure (Figure 2a) was obtained by relaxing the domain walls under constrained shape/volume conditions. Periodic boundary conditions were applied to the end faces of the supercell.

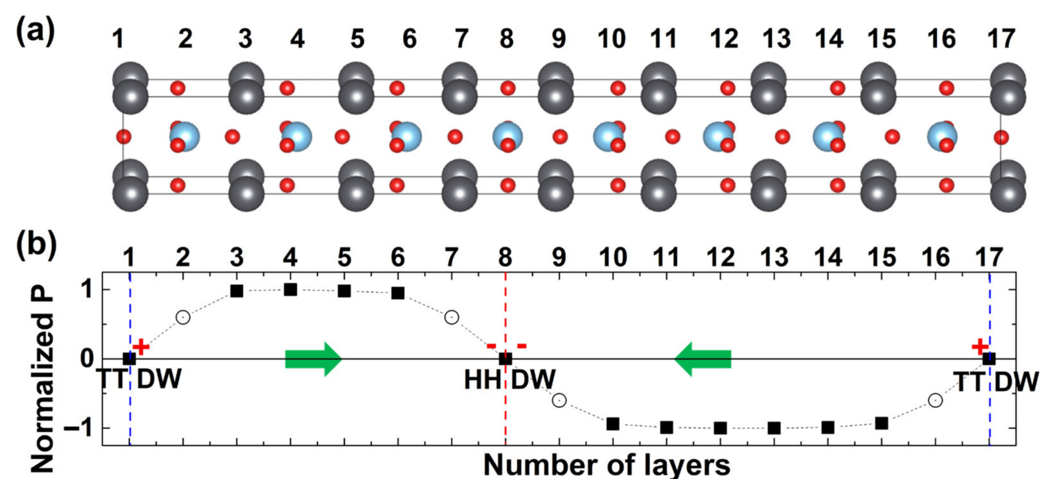

Figure 2. (**a**) Relaxed structure containing both HH and TT 180° charged DWs (CDWs) and (**b**) normalized polarization profile of the periodic domain wall structure shown in (**a**). The black squares represent normalized polarization of an individual layer, calculated using Born effective charges. The open circles indicate estimated values. The vertical dashed line indicates the DW position (red: HH CDW; blue: TT CDW). The vertical dotted lines depict the positions of the TiO_2 layer (red) and the PbO layers (blue). The flat plateaus at the center of each domain represent a polarization of ±136.5 μC/cm^2. The green arrows depict the direction of the macroscopic polarization within each domain; the + and − signs denote the sign of the polarization-induced charges at the TT and HH CDWs.

Boltzmann transport theory, with the relaxation time approximation [43], was employed to calculate the electronic transport properties. In semiconductors, conductivity (σ) is expressed as:

$$\sigma = en\mu_{\mathrm{n}} + ep\mu_{\mathrm{p}}, \quad (1)$$

where e is the elementary charge, μ_{n} (μ_{p}) denotes the mobilities of the electrons (holes), and n (p) signifies their concentrations. Carrier concentration was determined using the Fermi–Dirac distribution for the occupation of Kohn–Sham electronic eigenstates at room temperature. The values for n and p were calculated from the density of states using the following formulas [44]:

$$n(T,u) = \frac{2}{\Omega} \iint_{BZ} f_0(T,\varepsilon,u)D(\varepsilon)d\varepsilon, \quad (2)$$

$$p(T,u) = \frac{2}{\Omega} \iint_{BZ} [1 - f_0(T,\varepsilon,u)]D(\varepsilon)d\varepsilon, \quad (3)$$

where Ω is the unit cell volume, f_0 is the Fermi–Dirac distribution, u is the chemical potential, ε is the electron energy, and $D(\varepsilon)$ is the density of states (DOS). The Drude model, within the framework of effective mass theory, describes carrier mobility as $\mu = e\tau/m^*$, where τ is the relaxation time during which electrons lose momentum due to scattering from defects, impurities, or vibrations (phonons) [45], and m^* is the carrier's effective mass. Accounting for anisotropy, mobility in the β direction (μ_β) can be expressed as:

$$\mu_\beta = e\langle\tau_\beta\rangle/m^*, \quad (4)$$

where $\langle\tau_\beta\rangle$ is the average relaxation time for the β direction [46]. This relationship allows us to calculate mobility upon obtaining the effective mass and average relaxation time. The effective mass of carriers is calculated based on the band structure of the five-atom unit cell of $PbTiO_3$, incorporating structural distortions and strains extracted from the HH or TTDW regions. Under an external electric field (treated classically), the effective mass is defined by: $m^*_{\alpha\beta} = \hbar^2[\partial^2\varepsilon_i(\vec{k})/\partial k_\alpha \partial k_\beta]^{-1}$, where α and β represent reciprocal lattice vector components, $\varepsilon_i(\vec{k})$ is the dispersion relation for the ith band, and $\hbar$ is the reduced Planck's constant. The required derivatives are evaluated numerically using a finite difference method (five-point stencil) [47]. This method offers high accuracy of $O(h^4)$ and avoids limitations associated with the single parabolic band approximation [46]. Determining the relaxation time is a more complex process and will be outlined in detail in a separate section.

The probability at which electrons scatter due to imperfections in the material determines their relaxation time. A higher scattering probability translates to a shorter relaxation time and lower mobility. Fermi's golden rule was employed to calculate the probability of an electron transitioning from an initial state (i, $\vec{k}$) to a final state (j, $\vec{k}'$) after a scattering event [46]:

$$\frac{1}{\tau(i,\vec{k})} = \frac{2\pi}{\hbar} \sum_{\vec{k}',j} |M(i\vec{k}, j\vec{k}')|^2 \delta[\varepsilon_i(\vec{k}) - \varepsilon_j(\vec{k}')]. \quad (5)$$

Here, i and j represent band indexes, $\vec{k}$, $\vec{k}'$ are electron wavevectors, ε is the electron energy, δ is the Dirac delta function, and $M(i\vec{k}, j\vec{k}')$ is the scattering matrix element. The scattering matrix element ($M(i\vec{k}, j\vec{k}') = \langle j, \vec{k}'|\Delta V|i, \vec{k}\rangle$) describes scattering from state (i, $\vec{k}$) to state (j, $\vec{k}'$) by the deviation potential arising from atomic displacement associated with phonons or the perturbation potential caused by defects or impurities. This equation applies to perfectly elastic scattering events [43] where electrons maintain their energy. For relaxation time in a specific field direction β (τ_β), the equation is adjusted by a weighting factor that accounts for the scattering angle. This factor is represented by $1 - v_\beta(j, \vec{k}')/v_\beta(i, \vec{k})$, where v_β ($= \partial\varepsilon(\vec{k})/\hbar\partial \vec{k}_\beta$) is the group velocity [48]. Calculating

the scattering matrix element is a key challenge. Let us focus on the dominant scattering mechanism: electron–phonon interactions, specifically with acoustic phonons. In this case, the scattering matrix element depends on the deformation potential (DP) of the material. DP theory assumes a linear relationship between the change in the lattice potential and the volume change caused by thermal motions [49]. When considering only acoustic phonons, the matrix element for scattering an electron (or hole) from state $|i,\vec{k}\rangle$ to $|i,\vec{k}'\rangle$ is expressed as: $|M(i\vec{k},j\vec{k}')|^2 = |j,\vec{k}'|\Delta V|i,\vec{k}|^2 = \left(E_1^i\right)^2 q^2 a_{\vec{q}}^2/N$, where $\vec{q} = \pm(\vec{k}' - \vec{k})$. At high temperatures where lattice waves are fully excited, the amplitude of the wave is given by: $a_{\vec{q}}^2 = k_B T/\left(2mq^2 v_a^2\right)$, where $\vec{v}_a$ is the velocity of the acoustic wave, m is the total mass of the lattice per unit volume, k_B is the Boltzmann constant, and T is the temperature. Finally, the average scattering probability is obtained by averaging the squared matrix element [46,49]: $|\langle M(i\vec{k},j\vec{k}')|^2\rangle = k_B T (E_\beta^i)^2/C_\beta$, where $C_\beta = \rho v_a^2 = N m v_a^2$ is the elastic constant for longitudinal strain in the propagation direction of the longitudinal acoustic (LA) wave (β) and ρ is the mass density. E_β^i is the DP constant of the i-th band. The DP constant, E_β^i, and the elastic constant, C_β, are crucial parameters for calculating the average scattering probability. C_β can be calculated using a total-energy versus a strain approach. Here, the crystal volume is isotropically deformed by $\pm1\%$ to determine its response to strain. E_β^i represents the shift in the band edge (valence band maximum or conduction band minimum) per unit strain [46,50–52].

3. Results and Discussion

Relaxing the eight-unit cell domain wall structure resulted in an unexpected outcome: the most stable configuration lacked the desired HH and TT CDWs and reverted to a centrosymmetric unpolarized structure [53]. However, by partially constraining the structure, a meta-stable state that contained the targeted CDWs is achieved, as illustrated in Figure 2a. The meta-stable structure exhibited lattice parameters of a = 3.822 Å, b = 3.822 Å, and c = 33.778 Å for the entire eight-unit supercell. In terms of a single unit cell, these dimensions translate to a = 3.822 Å, b = 3.822 Å, and c = 4.222 Å. Notably, the typical lattice parameters for unconstrained bulk $PbTiO_3$ are a = 3.88 Å, b = 3.88 Å, and c = 4.29 Å. This comparison reveals that the simulations used required a slight compressive strain (approximately 1.5%) to be applied in all directions to achieve a stable configuration. This suggests that the system is effectively under high hydrostatic pressure. The numbering scheme in Figure 2a corresponds to the stacking order of atomic layers within the crystal structure. For instance, '1' represents the PbO layer on the left-hand side, and '2' represents the adjacent TiO_2 layer.

Figure 2b presents the calculated layer-by-layer effective polarization profile within the eight-unit $PbTiO_3$ supercell containing alternating 180° HH and TT CDWs. The Born effective charge method is used to estimate the polarization for each layer. The profile exhibits a remarkably flat polarization plateau within the domain interiors (about 136.5 μC cm^{-2}). This value exceeds those previously reported (45–92 μC cm^{-2}) [53,54] but remains lower than the giant polarization observed in super-tetragonal $PbTiO_3$ thin films (236.3 μC cm^{-2}) [55]. Although the chosen PBE functional might slightly overestimate polarization [56], the dominant factor is the compressive strain, consistent with findings that high pressure enhances $PbTiO_3$'s ferroelectricity through electronic mechanisms, not traditional ionic ones [57,58]. The authors propose that pressure alters the balance between long-range Coulomb interactions and short-range electronic effects. Beyond a critical point, $PbTiO_3$ becomes more ferroelectric to minimize the overlap between the Ti 3d and O 2s orbitals, naturally increasing due to pressure-induced contraction [57]. At the DWs, the polarization deviates from the constant value due to localized, strong, and non-homogeneous atomic distortions. As shown in Figure 2b, the HHDW exhibits zero net polarization at the central TiO_2 layer, unlike a previous study where the PbO layer displayed this behavior [53]. This discrepancy can arise from the differing boundary conditions, with the prior study

including a vacuum on one end. For TTDWs, the zero net polarization layer is the edge PbO layer. These non-uniform polarization regions span roughly two-unit cells, allowing estimation of a surprisingly small DW width of only two-unit cells—significantly smaller than previous results [53]. Specifically, as depicted in Figure 2, the HHDW encompasses layers 6–10, while the TTDW involves layers 1–3 and 15–16. This predicted thickness aligns well with the prior theoretical prediction of 10^{-7} cm [59] but remains smaller than the six-unit cell DW width reported by Sifuna et al. [53] The underlying physical mechanism for stabilizing this intrinsic domain wall and achieving such a small width is an intriguing question.

Opposing polarization vectors within these 180° DWs generate bound charges, creating a localized region of high electrostatic energy and inherent instability. However, Figure 2 demonstrates a stable domain structure, suggesting an intrinsic screening mechanism for the bound charges. The current study calculations, absent of defects or dopants, reveal that this screening mechanism in $PbTiO_3$ DWs involves electronic reconstruction leading to the formation of a two-dimensional electron/hole gas [53]. The accumulation of electrons or holes at the DWs effectively neutralizes the bound charges, resulting in the formation of thin, quasi-two-dimensional conductive layers. Subsequent analysis of carrier concentration at the domain walls further supports this conclusion. A critical question persists: what mechanism governs the generation of free carriers that perfectly screen the domain wall's polarization charges?

Figure 3 depicts the layer-resolved partial density of states (PDOS) for the atomic orbitals of Ti and O in the TiO_2 layers and Pb and O in the PbO layers of the eight-unit $PbTiO_3$ supercell containing HHDWs and TTDWs. The energy scale is shown in electron volts (eVs), with the Fermi level (E_F) set to 0 eV for reference. Consistent with the labeling, the bottom curve corresponds to the first layer (PbO), and the top curve corresponds to the 16th layer (TiO_2). Notably, all layers exhibit a pseudo energy gap, despite variations in the Fermi level position.

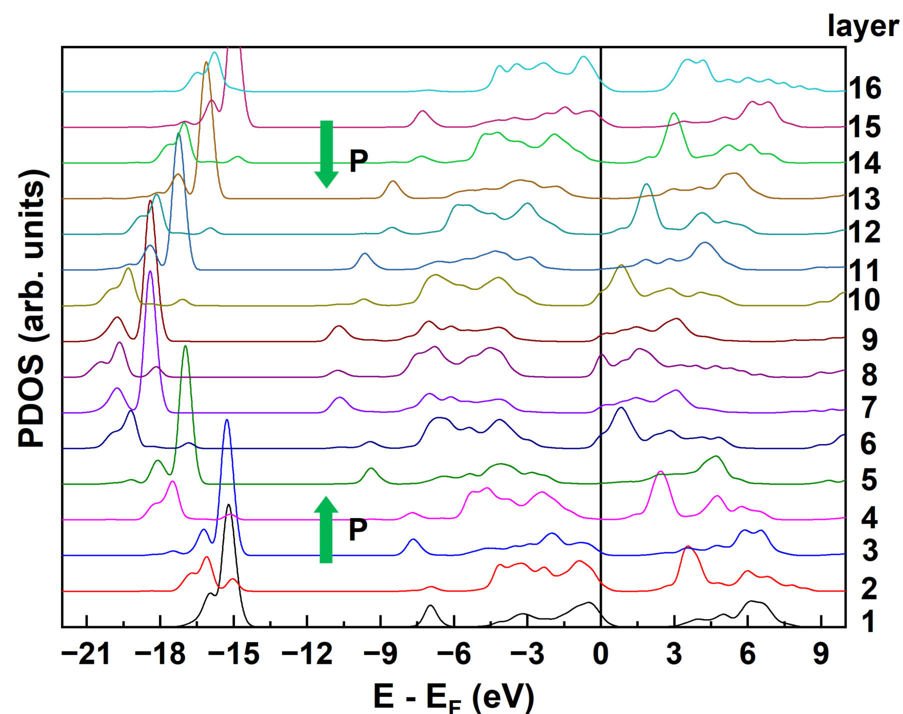

Figure 3. Layer-by-layer partial density of states (PDOS) for the eight-unit $PbTiO_3$ supercell containing HHDWs and TTDWs. The bottom curve corresponds to the first layer (PbO), and the top curve corresponds to the 16th layer (TiO_2). The vertical black line at zero energy indicates the Fermi level, E_F. The green arrow denotes the direction of the polarization within the domain.

Figures 4 and 5 depict the electronic structure of the HH and TT CDWs in the $PbTiO_3$ supercell, respectively. They present both the total DOS and the PDOS for each atomic species within the DW region. Below the E_F, the bands in both figures primarily from O 2p orbitals. Above the E_F, these bands arise from the hybridization of O 2p, Ti 3d, and Pb 6p orbitals. The position of the E_F is critical for understanding the electronic properties. In the HH CDWs (Figure 4), the E_F lies above the bottom of the conduction band, leading to a partially filled conduction band and a degenerate electronic state. This state is further supported by the non-vanishing PDOS at the E_F, indicating the presence of free electrons. These electrons may originate from the TT CDWs, as evidenced by the crossing of the E_F with the PDOS at the valence band top in Figure 5. This suggests the formation of holes (missing electrons) at the TT CDWs. Conversely, in the TT CDWs (Figure 5), the E_F falls within the band gap, specifically below the top of the valence band. This positioning also contributes to a degenerate state with holes populating the top of the valence band. These holes seem to originate from the transfer of electrons to the HH CDWs, as observed in Figure 4. The local metallization is confined to the CDW region. Moving away from the interface, the PDOS of both the conduction and valence bands converge rapidly towards their bulk counterparts and nearly vanish at the Fermi level, indicating a return to semiconductor behavior. Furthermore, the observed rigid shift in the PDOS of each layer suggests the presence of an internal remnant depolarization field. This field acts to electrostatically confine the free charges within the CDW region [60]. As shown in Figure 6, the bending of the energy bands can be influenced by this field, playing a crucial role in determining the atomic orbitals involved in the electronic reconstruction [53].

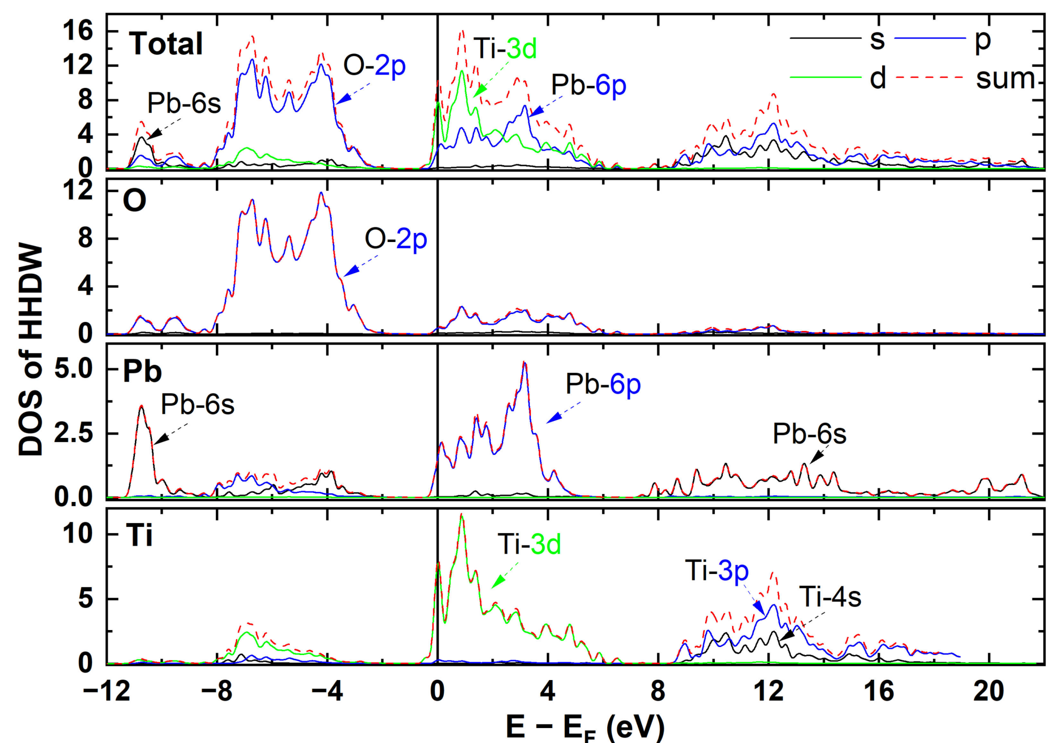

Figure 4. The DOS for head-to-head domain walls in a $PbTiO_3$ supercell, along with the PDOS for each type of atom within the domain wall.

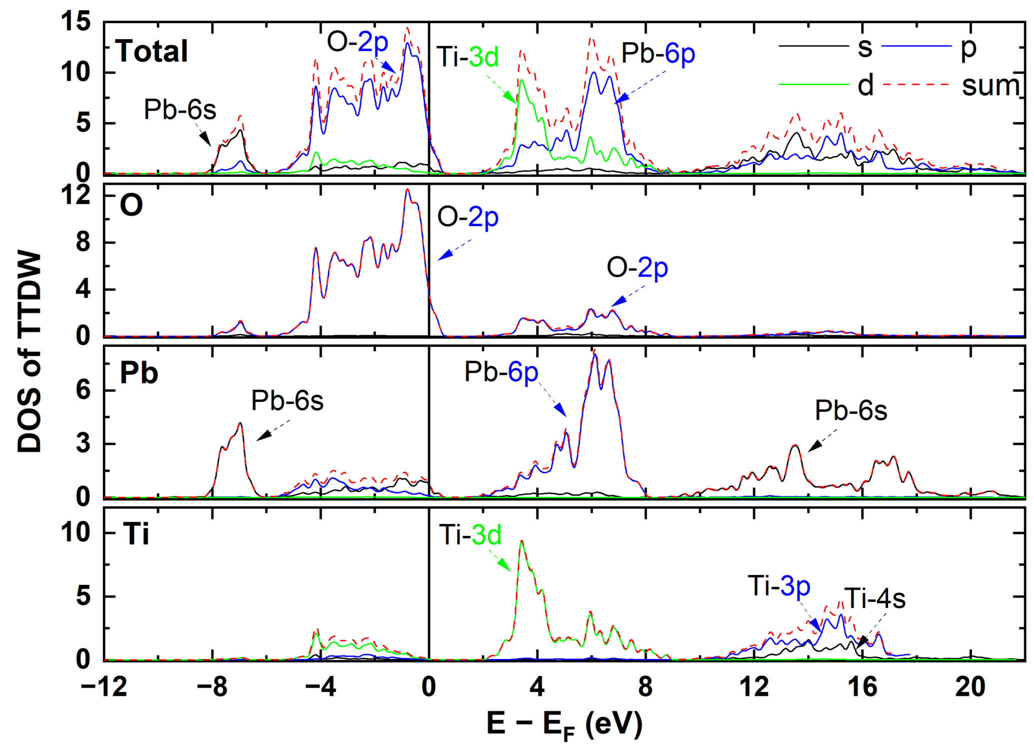

Figure 5. The DOS for tail-to-tail domain walls in a $PbTiO_3$ supercell, along with the PDOS for each type of atom within the domain wall.

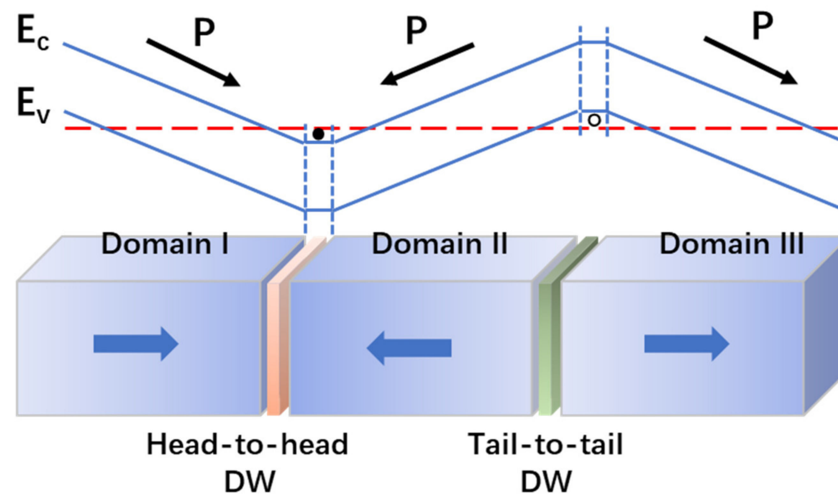

Figure 6. Energy band diagram of the periodic 180° charged domain walls. E_c and E_v denote the conduction and valence band edges, respectively. The arrows indicate the direction of macroscopic polarization (P) within each domain. The red dashed line represents the Fermi level. The black dot represents the localization of free electrons within the head-to-head domain wall, while the open circle represents the localization of holes within the tail-to-tail domain wall.

Building upon the electronic structure analysis (Figures 3–5), one can now investigate the distribution and origin of charge carriers within CDWs. Semiconductor theory dictates that the concentration of electrons depends on the DOS near the conduction band minimum, while the hole concentration relies on the DOS near the valence band maximum. Figures 4 and 5 offer deeper insights by decomposing the orbital contributions to these electron and hole charges. Analysis reveals that, in the HH CDW (Figure 4), the electron gas primarily originates from Ti 3d orbitals, with a minor contribution from Pb 6p orbitals. Conversely, the TT CDW (Figure 5) exhibits a hole gas mainly composed of O 2p orbitals

from both the PbO and the TiO_2 layers. These findings support the concept of electronic reconstruction at the CDWs to screen the polarization charges [16,30]. The discontinuity in polarization at the DWs acts as the driving force for this reconstruction. Charge transfer between HH and TT CDWs further enhances screening, stabilizing the overall two-CDW configuration. Both CDWs exhibit localization effects due to the remnant electric potential energy within the domains. As depicted in Figure 6, these potentials ($\vee$ for HH and $\wedge$ for TT) confine the respective carriers (electrons for HH and holes for TT) within potential wells. Within these wells, a stable, degenerate electron (or hole) gas forms, effectively screening the polarization divergences in the corresponding CDW [61]. This scenario involves a significant amount of free charge populating the band edges.

To quantify the charge transfer between HH and TT CDWs for screening purposes, one can calculate the concentration of free carriers (electrons and holes) within each layer of PbO and TiO_2 in the periodic DW structure (Figure 7a). Within the framework of band theory, the distribution of free carriers in ferroelectric semiconductors follows the temperature-dependent Fermi–Dirac distribution. As temperature increases, the number of free carriers increases, leading to a rise in intrinsic conductivity. Here, the Fermi–Dirac distribution was employed to account for the occupancy of Kohn–Sham electronic eigenstates, assuming a room temperature of 300 K for both the HH and TT configurations. These calculations indicate that an electron (or hole) concentration of approximately 10^{21}~10^{22} cm^{-3} is necessary for effective screening of the HH (TT) walls in the $PbTiO_3$ supercell. This carrier concentration aligns with previous reports by Vul et al. (10^{21} cm^{-3}) and Sifuna et al. (10^{21}–10^{22} cm^{-3}) [53,59]. To confirm the observed non-local charge neutrality of the DW system, one can integrate the average free charge densities profiles along the (001) direction. This integration provides the total free carrier concentration per unit volume (n and p). The HH CDW exhibits an additional electron concentration populating the bottom of the conduction band, quantified as $n^{HH} = 1.16 \times 10^{22}$ electrons cm^{-3} (Figure 7a). These electrons seem to originate from the TT CDW, where the integration of the free hole charge profile yields a value of $p^{TT} = 8.69 \times 10^{21}$ holes cm^{-3}. This observation aligns with the global charge neutrality condition, which dictates that $n^{HH}\Omega_{DW}^{HH} = p^{TT}\Omega_{DW}^{TT}$, where Ω_{DW} represents the volume of the CDWs. In simpler terms, the additional holes at the TT CDWs balance the extra electrons populating the conduction band at the HH CDWs, maintaining overall electrical neutrality [53].

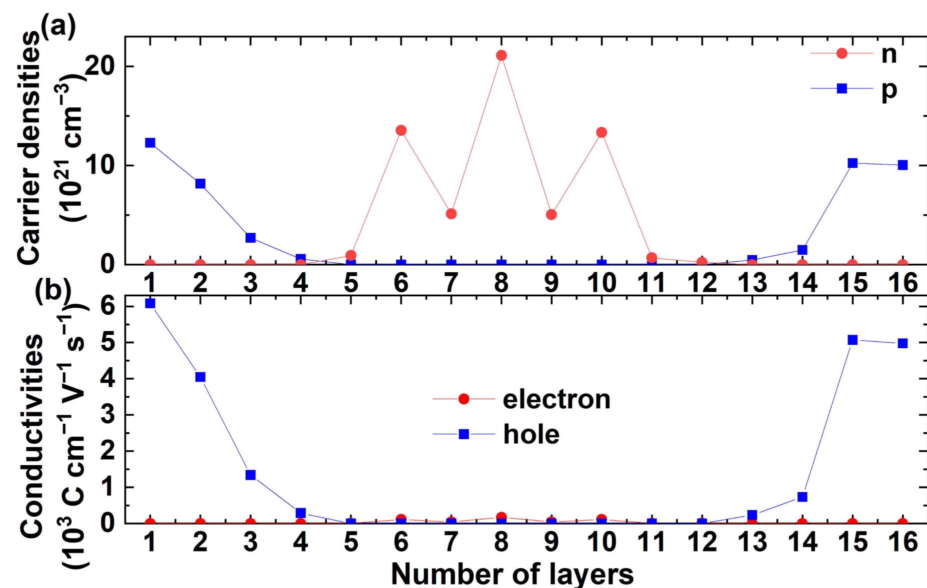

Figure 7. Free carrier distribution (**a**) and conductivity (**b**) in the eight-unit $PbTiO_3$ supercell containing HHDWs and TTDWs. Blue squares in (**a**) represent the concentration of holes (p) in each layer, while red dots represent the free electron concentration (n). Blue squares in (**b**) represent the hole conductivity, and red dots represent the free electron conductivity for each layer.

The electronic transport properties of the CDWs are calculated using Boltzmann transport theory, effective mass theory, and the relaxation time approximation. The results reveal a mobility of 5.09×10^{-2} cm^2 V^{-1} s^{-1} for electrons in the HH CDW (Table 1). This value aligns with the free carrier mobility of 1.49×10^{-2} cm^2 V^{-1} s^{-1} reported for the CDW region in $BiFeO_3$ [35]. In contrast, the calculated hole mobility for the TT CDW is significantly higher, at 3.09 cm^2 V^{-1} s^{-1}. Figure 7b presents the calculated conductivities for each layer of the $PbTiO_3$ supercell containing both HH and TT CDWs. The average electron conductivity at the HH CDW is 9.48×10^3 S m^{-1}, while the average hole conductivity at the TT CDW is 5.05×10^5 S m^{-1}. Notably, the calculated conductivity of the DWs, ranging from 10^3 to 10^5 S m^{-1}, is significantly higher than the conductivity of the typical semiconductor silicon (4.35×10^{-4} S m^{-1}). This finding confirms good enough CDW conduction, although it remains lower than the conductivity of a typical metal like gold (4.11×10^7 S m^{-1}). As shown in Figure 7b, the hole conductance from the TT CDWs is ten times greater than the electron conductance from the HH CDWs. This difference primarily arises from the larger hole mobility observed at the TT CDWs. Similar observations of significantly higher TT CDW conductance compared to HH CDW conductance have been reported for $ErMnO_3$ CDWs [24]. A comprehensive analysis reveals that domain wall conductance originates from the accumulation of charge carriers, with carrier concentration playing a crucial role. However, the difference in conductance between HH CDWs and TT CDWs is primarily driven by the disparity in carrier mobility.

Table 1. Mobilities (μs) and density-of-states effective masses (ms)for electrons and holes at the HHDW and TTDW. m_e denotes the mass of the free electron. The density-of-states effective masses can be calculated using the following formula: $m_d^* = (m_x^* \cdot m_y^* \cdot m_z^*)^{1/3}$, where m_x^*, m_y^*, and m_z^* represent the effective masses along the x, y, and z directions, respectively.

	HHDW	TTDW
μ^n [cm^2 V^{-1} s^{-1}]	5.09×10^{-2}	5.16×10^{-4}
μ^p [cm^2 V^{-1} s^{-1}]	1.18	3.09
m_d^{*n} [m_e]	26.27	33.79
m_d^{*p} [m_e]	1.99	1.82

Traditionally, CDWs display metallic-like conductivity, but this property is often hampered by inherent instability. This instability arises from the high electrostatic energy associated with bound charges induced by polarization within the CDW [62]. To achieve stability and a robust domain wall structure, a sufficiently high density of free carriers is necessary to screen the bound charges. However, attaining this density in practical materials often proves challenging, leading to a reliance on defects for DW stabilization [7]. Stable, naturally occurring ferroelectric CDWs have only been observed in specific improper ferroelectrics like $YMnO_3$ [63] and $ErMnO_3$ [24]. However, recent studies suggest that CDWs can form in defect-free $PbTiO_3$ ferroelectrics with sufficiently thick domains [53,61]. The current research indicates the formation of stable charged HHDWs and TTDWs in defect-free, nanoscale $PbTiO_3$ under high pressure. These intrinsic CDWs achieve stability via self-generated free carriers, eliminating the need for external defects [59,61,64]. The system considered here exhibits remarkable stability despite the absence of external defects. Two key factors contribute to this: a lowered carrier generation barrier and the coexistence of opposite-sign carriers. While the overall band gap shape remains largely intact (Figure 3), a non-zero, but extremely low, DOS persists at the band gap bottom. The near-zero DOS suggests an extremely low concentration of free carriers, resulting in weak metallicity. The ferroelectricity is evidenced by the large polarization calculated in this paper and supported by existing literature [57,58]. Notably, ferroelectricity and metallicity can coexist, as observed in ferroelectric metals, with the potential for exciting applications [65–67]. Unlike traditional metals with only electrons, $PbTiO_3$ under high pressure seems possessing both electrons and holes due to the covalent nature of Pb–O and Ti–O bonds (Figures 4 and 5). When an electron breaks free from a covalent bond, it leaves

behind a hole. Conversely, consider a hypothetical scenario where a high-pressure environment transforms the covalent bond into a metallic bond, as described by the Drude model with its sole reliance on electron carriers. In such a metallic scenario, an accumulation of electrons at the HHDW due to the shielding of its polarization. However, the TTDW would retain its negative polarization without a corresponding positive counterpart (hole). This inherent imbalance in charge distribution signifies an unstable system, contradicting the calculated stability observed in this study. The presence of holes is crucial for maintaining electrostatic balance within the system [68]. High pressure creates this non-zero DOS in the band gap, indicating weak metallicity, and eliminates the forbidden band, reducing the energy barrier for the generation of electron-hole pairs. This facilitates the creation of free carriers that can screen the bound charges. However, the extremely low DOS limits the overall carrier concentration, resulting in quite weak metallicity. This aligns with the carrier concentration, which matches values reported for relaxed single-DW systems [53], indicating that relatively high pressure does not significantly increase carrier numbers. This suggests a critical state between semiconducting and metallic behavior, leading to a semiconductor-like system with quite a small number of electrons and holes. The ultra-low DOS in the pseudo-band gap justifies the use of semiconductor theory for analysis. In summary, the stability of the high-pressure defect-free system arises from a combination of preserved band gap character, weak metallicity, and the presence of electron–hole pairs. As experimentally observed, smaller band gaps lead to more stable CDWs [21,69]. In this case, the weak metallicity of system used here accelerates the stabilization of small-scale domain walls.

For traditional semiconductors, such as silicon, germanium, and gallium arsenide, the mobility of electrons is greater than the mobility of holes [68]. However, in both HHDWs and TTDWs, the carrier mobility is larger for the holes than for the electrons, as shown in Table 1. Let us attribute this behavior to the anisotropic nature of the effective mass for electrons and holes within the domain wall structures. The effective masses of electrons and holes at both DWs are referenced in Table 2. At the HHDW, the electron effective mass perpendicular to the domain wall plane (out-plane effective mass, m^*_{nz}) is significantly larger (four orders of magnitude) compared to the in-plane effective mass (m^*_{nx} and m^*_{ny}). This substantial increase suggests that electrons encounter significant difficulty moving perpendicular to the domain wall. The underlying reason is that the volume of the unit cell at HHDW shrinks along the out-plane direction due to HH polarization. In the HHDW region, the lattice constant c = 4.042 Å, while in the TTDW region, the lattice constant c = 4.626 Å. It is understandable that the size of the unit cell at the HHDW is significantly smaller than that at the TTDW. This volume reduction leads to a higher probability of electron scattering, consequently increasing the effective mass. Considering all three dimensions, the large m^*_{nz} contributes to a higher density-of-states effective mass m^*_d for electrons at the HHDW, as shown in Table 1. A larger m^*_d translates to a lower average scattering time ($\langle\tau\rangle$), ultimately reducing electron mobility. Conversely, holes in the HHDW exhibit a lower effective mass in the out-plane direction compared to the in-plane direction. This allows for quite easier hole movement perpendicular to the domain wall. Additionally, the lower density-of-states effective mass for holes (about $2m_e$) further enhances their mobility. In contrast to the HHDW region, the TTDW region experiences a volume expansion along the direction perpendicular to the domain wall due to the reversed polarization direction. This creates a more favorable pathway for electron movement in the out-plane direction, where they have a lower effective mass. However, the in-plane effective mass of electrons within the TTDW remains relatively high, resulting in a large density-of-states effective mass (33.79 m_e) and, consequently, lower mobility. The lattice distortion at the TTDW also introduces anisotropy in the hole's effective mass, with different values in all three directions. The highest value (m^*_{pz}) indicates a greater impediment for hole motion perpendicular to the domain wall compared to other directions. However, the overall density-of-states effective mass for holes remains relatively low, and the effective masses

in all directions are not significantly high. This combination leads to a higher mobility for holes compared to electrons in both DWs.

Table 2. Effective masses of electrons and holes at the HHDW and TTDW, and their components in three coordinate directions.

	m_n^* (m_e)			m_p^* (m_e)		
	m_{nx}^*	m_{ny}^*	m_{nz}^*	m_{px}^*	m_{py}^*	m_{pz}^*
HHDW	1.54	1.54	7652.39	3.26	3.26	0.75
TTDW	104.01	101.45	3.66	1.42	0.66	6.48

The existence of "strongly correlated" CDWs, like those observed in $PbTiO_3$, hinges on near-perfect compensation of polarization charges. This compensation leads to the formation of a degenerate, quasi-two-dimensional electron gas exhibiting metallic-like carrier concentrations [7]. The potential applications for CDWs are vast, but significant hurdles remain in translating this potential into practical devices. One promising approach involves "frustrated poling" techniques to create stable CDWs during device fabrication [7,70]. However, careful selection of electrode materials is critical. Here, the contact potential difference between the ferroelectric and metal electrodes plays a crucial role, and it is directly influenced by the work function difference of the materials involved [59]. Additionally, the inherent coupling between ferroelectric and ferroelastic domain states can be harnessed for the design and creation of stable CDWs [7]. This study offers valuable insights into achieving stable CDWs. The studied system, under hydrostatic pressure, undergoes a pressure-induced metallization transition. At the critical state of this transition, electron–hole pairs are readily generated, effectively shielding the domain wall charge and promoting its stability. This suggests that hydrostatic pressure can be a powerful tool for generating stable charged intrinsic domain walls in $PbTiO_3$-like materials. This paper presents a novel approach to generating stable CDWs without relying on defects.

4. Conclusions

This paper introduces a novel first-principles method that incorporates Boltzmann transport theory and relaxation time approximation to calculate the carrier concentration, mobility, and conductivity of DWs with both 180° HH and TT polarization configurations. Simulations demonstrate stabilization of HH and TT CDWs within a periodic DW configuration in a $PbTiO_3$ system under hydrostatic pressure. This stabilization is attributed to electrostatic screening by free carriers, whose generation is facilitated by compressive strain. This screening process involves the transfer of electrons from the TTDW to the HHDW, leading to the formation of quasi-two-dimensional electron and hole gases. The developed model was used to determine the carrier concentration, mobility, and conductivity for both CDWs within the eight-unit $PbTiO_3$ supercell. The HH CDW exhibited a conductivity of 9.48×10^3 S m^{-1}, with an electron concentration of 1.16×10^{22} electrons cm^{-3} and an electron mobility of 5.09×10^{-2} cm^2 V^{-1} s^{-1}. In comparison, the TT CDW displayed a significantly higher hole conductivity of 5.05×10^5 S m^{-1}, with a hole concentration of 8.69×10^{21} holes cm^{-3} and a hole mobility of 3.09 cm^2 V^{-1} s^{-1}. While both CDWs exhibit good conductivity, the TT CDW displays a significantly higher value compared to the HH CDW. Systematic investigation revealed that the accumulation of free carriers, particularly their concentration, plays a dominant role in the CDW conductance mechanism. However, the observed difference in conductance between HH and TT CDWs primarily arises from the difference in carrier mobility. These findings provide valuable insights into the carrier transport mechanisms within ferroelectric DW devices. In summary, a powerful first-principles method has been proposed for calculating the conductivity of ferroelectric CDWs, applicable to a wide range of ferroelectric materials and their corresponding CDW devices. Furthermore, this study suggests that reducing the band gap (e.g., via hydrostatic pressure as applied to $PbTiO_3$) offers a powerful strategy for stabilizing charged

domain walls. These results offer significant advancements in the understanding of the internal mechanisms governing these devices and pave the way for their optimization and future applications.

Funding: The work was supported in part by funding from the Natural Science Foundation of Shandong Province (No. ZR201702120113), National Natural Science Foundation of China (No. 11104116), and the Distinguished Middle-Aged and Young Scientist Encourage and Reward Foundation of Shandong Province (No. BS2011CL003).

Data Availability Statement: Data are contained within the article.

Conflicts of Interest: The author declares no conflicts of interest.

References

1. Martin, L.W.; Rappe, A.M. Thin-film ferroelectric materials and their applications. *Nat. Rev. Mater.* **2016**, *2*, 16087. [CrossRef]
2. Seidel, J.; Martin, L.W.; He, Q.; Zhan, Q.; Chu, Y.H.; Rother, A.; Hawkridge, M.; Maksymovych, P.; Yu, P.; Gajek, M. Conduction at domain walls in oxide multiferroics. *Nat. Mater.* **2009**, *8*, 229–234. [CrossRef] [PubMed]
3. Salje, E.; Zhang, H. Domain boundary engineering. *Phase Transit.* **2009**, *82*, 452–469. [CrossRef]
4. Fäth, M.; Freisem, S.; Menovsky, A.A.; Tomioka, Y.; Aarts, J.; Mydosh, J.A. Spatially inhomogeneous metal-insulator transition in doped manganites. *Science* **1999**, *285*, 1540–1542. [CrossRef] [PubMed]
5. Seidel, J.; Trassin, M.; Zhang, Y.; Maksymovych, P.; Uhlig, T.; Milde, P.; Köhler, D.; Baddorf, A.P.; Kalinin, S.V.; Eng, L.M.; et al. Electronic properties of isosymmetric phase boundaries in highly strained Ca-doped $BiFeO_3$. *Adv. Mater.* **2014**, *26*, 4376–4380. [CrossRef] [PubMed]
6. Crassous, A.; Sluka, T.; Tagantsev, A.K.; Setter, N. Polarization charge as a reconfigurable quasi-dopant in ferroelectric thin films. *Nat. Nanotechnol.* **2015**, *10*, 614–618. [CrossRef]
7. Sluka, T.; Tagantsev, A.K.; Bednyakov, P.; Setter, N. Free-electron gas at charged domain walls in insulating $BaTiO_3$. *Nat. Commun.* **2013**, *4*, 1808. [CrossRef]
8. Schröder, M.; Haußmann, A.; Thiessen, A.; Soergel, E.; Woike, T.; Eng, L.M. Conducting domain walls in lithium niobate single crystals. *Adv. Funct. Mater.* **2012**, *22*, 3936–3944. [CrossRef]
9. Guyonnet, J.; Gaponenko, I.; Gariglio, S.; Paruch, P. Conduction at domain walls in insulating $Pb(Zr_{0.2}Ti_{0.8})O_3$ thin films. *Adv. Mater.* **2011**, *23*, 5377–5382. [CrossRef]
10. Kim, Y.; Alexe, M.; Salje, E.K.H. Nanoscale properties of thin twin walls and surface layers in piezoelectric WO_{3-x}. *Appl. Phys. Lett.* **2010**, *96*, 032904. [CrossRef]
11. Maksymovych, P.; Seidel, J.; Chu, Y.H.; Wu, P.; Baddorf, A.P.; Chen, L.Q.; Kalinin, S.V.; Ramesh, R. Dynamic conductivity of ferroelectric domain walls in $BiFeO_3$. *Nano Lett.* **2011**, *11*, 1906–1912. [CrossRef] [PubMed]
12. Bednyakov, P.S.; Sluka, T.; Tagantsev, A.K.; Damjanovic, D.; Setter, N. Formation of charged ferroelectric domain walls with controlled periodicity. *Sci. Rep.* **2015**, *5*, 15819. [CrossRef] [PubMed]
13. Beccard, H.; Beyreuther, E.; Kirbus, B.; Seddon, S.D.; Rüsing, M.; Eng, L.M. Hall mobilities and sheet carrier densities in a single $LiNbO_3$ conductive ferroelectric domain wall. *Phys. Rev. Appl.* **2023**, *20*, 064043. [CrossRef]
14. Seidel, J.; Fu, D.; Yang, S.Y.; Alarcón-Lladó, E.; Wu, J.; Ramesh, R.; Ager, J.W. Efficient photovoltaic current generation at ferroelectric domain walls. *Phys. Rev. Lett.* **2011**, *107*, 126805. [CrossRef]
15. McGilly, L.J.; Yudin, P.; Feigl, L.; Tagantsev, A.K.; Setter, N. Controlling domain wall motion in ferroelectric thin films. *Nat. Nanotechnol.* **2015**, *10*, 145–150. [CrossRef]
16. Catalan, G.; Seidel, J.; Ramesh, R.; Scott, J.F. Domain wall nanoelectronics. *Rev. Mod. Phys.* **2012**, *84*, 119–156. [CrossRef]
17. Maguire, J.R.; McCluskey, C.J.; Holsgrove, K.M.; Suna, A.; Kumar, A.; McQuaid, R.G.P.; Gregg, J.M. Ferroelectric Domain wall p–n j unctions. *Nano Lett.* **2023**, *23*, 10360–10366. [CrossRef]
18. Qian, Y.; Zhang, Y.; Xu, J.; Zhang, G. Domain-wall p-n junction in lithium niobate thin film on an insulator. *Phys. Rev. Appl.* **2022**, *17*, 044011. [CrossRef]
19. Sun, J.; Jiang, A.Q.; Sharma, P. Ferroelectric domain wall memory and logic. *ACS Appl. Electron. Mater.* **2023**, *5*, 4692–4703. [CrossRef]
20. Suna, A.; McCluskey, C.J.; Maguire, J.R.; Holsgrove, K.M.; Kumar, A.; McQuaid, R.G.P.; Gregg, J.M. Tuning local conductance to enable demonstrator ferroelectric domain wall diodes and logic gates. *Adv. Phys. Res.* **2023**, *2*, 2200095. [CrossRef]
21. Nataf, G.F.; Guennou, M.; Gregg, J.M.; Meier, D.; Hlinka, J.; Salje, E.K.H.; Kreisel, J. Domain-wall engineering and topological defects in ferroelectric and ferroelastic materials. *Nat. Rev. Phys.* **2020**, *2*, 634–648. [CrossRef]
22. Lubk, A.; Gemming, S.; Spaldin, N.A. First-principles study of ferroelectric domain walls in multiferroic bismuth ferrite. *Phys. Rev. B* **2009**, *80*, 104110. [CrossRef]
23. Chiu, Y.P.; Chen, Y.T.; Huang, B.C.; Shih, M.C.; Yang, J.C.; He, Q.; Liang, C.W.; Seidel, J.; Chen, Y.C.; Ramesh, R.; et al. Atomic-scale evolution of local electronic structure across multiferroic domain walls. *Adv. Mater.* **2011**, *23*, 1530–1534. [CrossRef]
24. Meier, D.; Seidel, J.; Cano, A.; Delaney, K.; Kumagai, Y.; Mostovoy, M.; Spaldin, N.A.; Ramesh, R.; Fiebig, M. Anisotropic conductance at improper ferroelectric domain walls. *Nat. Mater.* **2012**, *11*, 284–288. [CrossRef]

25. Vasudevan, R.K.; Morozovska, A.N.; Eliseev, E.A.; Britson, J.; Yang, J.C.; Chu, Y.H.; Maksymovych, P.; Chen, L.Q.; Nagarajan, V.; Kalinin, S.V. Domain wall geometry controls conduction in ferroelectrics. *Nano Lett.* **2012**, *12*, 5524–5531. [CrossRef]
26. Godau, C.; Kämpfe, T.; Thiessen, A.; Eng, L.M.; Haußmann, A. Enhancing the domain wall conductivity in lithium niobate single crystals. *ACS Nano* **2017**, *11*, 4816–4824. [CrossRef]
27. Farokhipoor, S.; Noheda, B. Conduction through 71° domain walls in $BiFeO_3$ thin films. *Phys. Rev. Lett.* **2011**, *107*, 127601. [CrossRef] [PubMed]
28. Seidel, J.; Maksymovych, P.; Batra, Y.; Katan, A.; Yang, S.Y.; He, Q.; Baddorf, A.P.; Kalinin, S.V.; Yang, C.H.; Yang, J.C.; et al. Domain wall conductivity in La-Doped $BiFeO_3$. *Phys. Rev. Lett.* **2010**, *105*, 197603. [CrossRef]
29. Rojac, T.; Bencan, A.; Drazic, G.; Sakamoto, N.; Ursic, H.; Jancar, B.; Tavcar, G.; Makarovic, M.; Walker, J.; Malic, B.; et al. Domain-wall conduction in ferroelectric $BiFeO_3$ controlled by accumulation of charged defects. *Nat. Mater.* **2017**, *16*, 322–327. [CrossRef] [PubMed]
30. Meier, D.; Selbach, S.M. Ferroelectric domain walls for nanotechnology. *Nat. Rev. Mater.* **2022**, *7*, 157–173. [CrossRef]
31. Campbell, M.P.; McConville, J.P.V.; McQuaid, R.G.P.; Prabhakaran, D.; Kumar, A.; Gregg, J.M. Hall effect in charged conducting ferroelectric domain walls. *Nat. Commun.* **2016**, *7*, 13764. [CrossRef] [PubMed]
32. Turner, P.W.; McConville, J.P.V.; McCartan, S.J.; Campbell, M.H.; Schaab, J.; McQuaid, R.G.P.; Kumar, A.; Gregg, J.M. Large carrier mobilities in $ErMnO_3$ conducting domain walls revealed by quantitative Hall-effect measurements. *Nano Lett.* **2018**, *18*, 6381–6386. [CrossRef] [PubMed]
33. McCluskey, C.J.; Colbear, M.G.; McConville, J.P.V.; McCartan, S.J.; Maguire, J.R.; Conroy, M.; Moore, K.; Harvey, A.; Trier, F.; Bangert, U.; et al. Ultrahigh carrier mobilities in ferroelectric domain wall corbino cones at room temperature. *Adv. Mater.* **2022**, *34*, 2204298. [CrossRef] [PubMed]
34. Beccard, H.; Kirbus, B.; Beyreuther, E.; Rüsing, M.; Bednyakov, P.; Hlinka, J.; Eng, L.M. Nanoscale conductive sheets in ferroelectric $BaTiO_3$: Large Hall electron mobilities at head-to-head domain walls. *ACS Appl. Nano Mater.* **2022**, *5*, 8717–8722. [CrossRef]
35. Chen, D.; Tan, X.; Shen, B.; Jiang, J. Erasable domain wall current-dominated resistive switching in $BiFeO_3$ devices with an oxide–metal interface. *ACS Appl. Mater. Inter.* **2023**, *15*, 25041–25048. [CrossRef]
36. Hohenberg, P.; Kohn, W. Inhomogeneous electron gas. *Phys. Rev. B* **1964**, *136*, 864–871. [CrossRef]
37. Kohn, W.; Sham, L. Self-consistent equations including exchange and correlation effects. *Phys. Rev.* **1965**, *140*, A1133. [CrossRef]
38. Kresse, G.; Furthmüller, J. Efficient iterative schemes for ab initio total-energy calculations using a plane-wave basis set. *Phys. Rev. B* **1996**, *54*, 11169. [CrossRef]
39. Kresse, G.; Furthmüller, J. Efficiency of ab-initio total energy calculations for metals and semiconductors using a plane-wave basis set. *Comp. Mater. Sci.* **1996**, *6*, 15–50. [CrossRef]
40. Kresse, G.; Hafner, J. Ab initio molecular dynamics for liquid metals. *Phys. Rev. B* **1993**, *47*, 558–561. [CrossRef]
41. Ceperley, D.M.; Alder, B.J. Ground state of the electron gas by a stochastic method. *Phys. Rev. Lett.* **1980**, *45*, 566–569. [CrossRef]
42. Perdew, J.P.; Burke, K.; Ernzerhof, M. Generalized gradient approximation made simple. *Phys. Rev. Lett.* **1996**, *77*, 3865–3868. [CrossRef] [PubMed]
43. Ganose, A.M.; Park, J.; Faghaninia, A.; Woods-Robinson, R.; Persson, K.A.; Jain, A. Efficient calculation of carrier scattering rates from first principles. *Nat. Commun.* **2021**, *12*, 2222. [CrossRef] [PubMed]
44. Madsen, G.K.; Carrete, J.; Verstraete, M.J. BoltzTraP2, a program for interpolating band structures and calculating semi-classical transport coefficients. *Comput. Phys. Commun.* **2018**, *231*, 140–145. [CrossRef]
45. Poncé, S.; Li, W.; Reichardt, S.; Giustino, F. First-principles calculations of charge carrier mobility and conductivity in bulk semiconductors and two-dimensional materials. *Rep. Prog. Phys.* **2020**, *83*, 036501. [CrossRef] [PubMed]
46. Xi, J.; Long, M.; Tang, L.; Wang, D.; Shuai, Z. First-principles prediction of charge mobility in carbon and organic nanomaterials. *Nanoscale* **2012**, *4*, 4348–4369. [CrossRef]
47. Abramowitz, M.; Stegun, I.A. (Eds.) *Handbook of Mathematical Functions. With Formulas, Graphs, and Mathematical Tables*; Dover Publications, Inc.: New York, NY, USA, 1972. Available online: https://archive.org/details/handbookofmathe000abra/ (accessed on 10 August 2024).
48. Harrison, W.A. Scattering of electrons by lattice vibrations in nonpolar crystals. *Phys. Rev.* **1956**, *104*, 1281–1290. [CrossRef]
49. Bardeen, J.; Shockley, W. Deformation potentials and mobilities in non-polar crystals. *Phys. Rev. Appl.* **1950**, *80*, 72–80. [CrossRef]
50. Sun, H.; Xu, Z.T.; Zhang, D. First-principles calculations to investigate doping effects on electrical conductivity and interfacial contact resistance of TiO_2. *Appl. Surf. Sci.* **2023**, *614*, 156202. [CrossRef]
51. Guechi, N.; Bouhemadou, A.; Medkour, Y.; Al-Douri, Y.; Khenata, R.; Bin-Omran, S. Electronic and thermoelectric properties of the layered Zintl phase CaIn2P2: First-principles calculations. *Philos. Mag.* **2020**, *100*, 3023–3039. [CrossRef]
52. Long, M.; Tang, L.; Wang, D.; Li, Y.; Shuai, Z. Electronic structure and carrier mobility in graphdiyne sheet and nanoribbons: Theoretical predictions. *ACS Nano* **2011**, *5*, 2593–2600. [CrossRef] [PubMed]
53. Sifuna, J.; García-Fernández, P.; Manyali, G.S.; Amolo, G.; Junquera, J. First-principles study of two-dimensional electron and hole gases at the head-to-head and tail-to-tail 180° domain walls in $PbTiO_3$ ferroelectric thin films. *Phys. Rev. B* **2020**, *101*, 174114. [CrossRef]
54. Meyer, B.; Vanderbilt, D. Ab initio study of ferroelectric domain walls in $PbTiO_3$. *Phys. Rev. B* **2002**, *65*, 104111. [CrossRef]
55. Zhang, L.; Chen, J.; Fan, L.; Diéguez, O.; Cao, J.; Pan, Z.; Wang, Y.; Wang, J.; Kim, M.; Deng, S. Giant polarization in super-tetragonal thin films through interphase strain. *Science* **2018**, *361*, 494–497. [CrossRef] [PubMed]

56. Junquera, J.; Ghosez, P. First-principles study of ferroelectric oxide epitaxial thin films and superlattices: Role of the mechanical and electrical boundary conditions. *J. Comput. Theor. Nanosci.* **2008**, *5*, 2071–2088. [CrossRef]
57. Kornev, I.A.; Bellaiche, L.; Bouvier, P.; Janolin, P.E.; Dkhil, B.; Kreisel, J. Ferroelectricity of perovskites under pressure. *Phys. Rev. Lett.* **2005**, *95*, 196804. [CrossRef]
58. Janolin, P.E.; Bouvier, P.; Kreisel, J.; Thomas, P.A.; Kornev, I.A.; Bellaïche, L.; Crichton, W.; Hanfland, M.; Dkhil, B. High-pressure effect on $PbTiO_3$: An investigation by Raman and X-ray scattering up to 63 GPa. *Phys. Rev. Lett.* **2008**, *101*, 237601. [CrossRef]
59. Vul, B.; Guro, G.; Ivanchik, I. Encountering domains in ferroelectrics. *Ferroelectrics* **1973**, *6*, 29–31. [CrossRef]
60. Stengel, M.; Aguado-Puente, P.; Spaldin, N.A.; Junquera, J. Band alignment at metal/ferroelectric interfaces: Insights and artifacts from first principles. *Phys. Rev. B* **2011**, *83*, 235112. [CrossRef]
61. Gureev, M.Y.; Tagantsev, A.K.; Setter, N. Head-to-head and tail-to-tail 180° domain walls in an isolated ferroelectric. *Phys. Rev. B* **2011**, *83*, 184104. [CrossRef]
62. Zhang, J.; Wang, Y.J.; Liu, J.; Xu, J.; Wang, D.; Wang, L.; Ma, X.L.; Jia, C.L.; Bellaiche, L. Origin of sawtooth domain walls in ferroelectrics. *Phys. Rev. B* **2020**, *101*, 060103. [CrossRef]
63. Choi, T.; Horibe, Y.; Yi, H.T.; Choi, Y.J.; Wu, W.; Cheong, S.W. Insulating interlocked ferroelectric and structural antiphase domain walls in multiferroic $YMnO_3$. *Nat. Mater.* **2010**, *9*, 253–258. [CrossRef]
64. Sluka, T.; Tagantsev, A.K.; Damjanovic, D.; Gureev, M.; Setter, N. Enhanced electromechanical response of ferroelectrics due to charged domain walls. *Nat. Commun.* **2012**, *3*, 748. [CrossRef]
65. Shi, Y.; Guo, Y.; Wang, X.; Princep, A.J.; Khalyavin, D.; Manuel, P.; Michiue, Y.; Sato, A.; Tsuda, K.; Yu, S. A ferroelectric-like structural transition in a metal. *Nat. Mater.* **2013**, *12*, 1024–1027. [CrossRef] [PubMed]
66. Peng, W.; Park, S.Y.; Roh, C.J.; Mun, J.; Ju, H.; Kim, J.; Ko, E.K.; Liang, Z.; Hahn, S.; Zhang, J. Flexoelectric polarizing and control of a ferromagnetic metal. *Nat. Phys.* **2024**, *20*, 450–455. [CrossRef]
67. Zhang, J.; Shen, S.; Puggioni, D.; Wang, M.; Sha, H.; Xu, X.; Lyu, Y.; Peng, H.; Xing, W.; Walters, L.N. A correlated ferromagnetic polar metal by design. *Nat. Mater.* **2024**, *23*, 912–919. [CrossRef]
68. Sze, S.M.; Li, Y.; Ng, K.K. *Physics of Semiconductor Devices*; John Wiley & Sons, Inc.: Hoboken, NJ, USA, 2021.
69. Liu, S.; Zheng, F.; Koocher, N.Z.; Takenaka, H.; Wang, F.; Rappe, A.M. Ferroelectric domain wall induced band gap reduction and charge separation in organometal halide perovskites. *J. Phys. Chem. Lett.* **2015**, *6*, 693–699. [CrossRef]
70. Wada, S.; Muraishi, T.; Yokoh, K.; Yako, K.; Kamemoto, H.; Tsurumi, T. Domain wall engineering in lead-free piezoelectric crystals. *Ferroelectrics* **2007**, *355*, 37–49. [CrossRef]

Disclaimer/Publisher's Note: The statements, opinions and data contained in all publications are solely those of the individual author(s) and contributor(s) and not of MDPI and/or the editor(s). MDPI and/or the editor(s) disclaim responsibility for any injury to people or property resulting from any ideas, methods, instructions or products referred to in the content.